Appl. Phys. A (2016) 122:270
DOI 10.1007/s00339-016-9829-9

Applied Physics A
Materials Science & Processing

Fabrication and characterization of boron-doped nanocrystalline diamond-coated MEMS probes

Robert Bogdanowicz[1] · Michał Sobaszek[1] · Mateusz Ficek[1] · Daniel Kopiec[2] · Magdalena Moczała[2] · Karolina Orłowska[2] · Mirosław Sawczak[3] · Teodor Gotszalk[2]

Received: 2 September 2015 / Accepted: 8 November 2015 / Published online: 7 March 2016

Abstract Fabrication processes of thin boron-doped nanocrystalline diamond (B-NCD) films on silicon-based micro- and nano-electromechanical structures have been investigated. B-NCD films were deposited using microwave plasma assisted chemical vapour deposition method. The variation in B-NCD morphology, structure and optical parameters was particularly investigated. The use of truncated cone-shaped substrate holder enabled to grow thin fully encapsulated nanocrystalline diamond film with a thickness of approx. 60 nm and RMS roughness of 17 nm. Raman spectra present the typical boron-doped nanocrystalline diamond line recorded at 1148 cm^{-1}. Moreover, the change in mechanical parameters of silicon cantilevers over-coated with boron-doped diamond films was investigated with laser vibrometer. The increase of resonance to frequency of over-coated cantilever is attributed to the change in spring constant caused by B-NCD coating. Topography and electrical parameters of boron-doped diamond films were investigated by tapping mode AFM and electrical mode of AFM–Kelvin probe force microscopy (KPFM). The crystallite–grain size was recorded at 153 and 238 nm for boron-doped film and undoped, respectively. Based on the contact potential difference data from the KPFM measurements, the work function of diamond layers was estimated. For the undoped diamond films, average CPD of 650 mV and for boron-doped layer 155 mV were achieved. Based on CPD values, the values of work functions were calculated as 4.65 and 5.15 eV for doped and undoped diamond film, respectively. Boron doping increases the carrier density and the conductivity of the material and, consequently, the Fermi level.

✉ Mateusz Ficek
mateuszficek@gmail.com

Robert Bogdanowicz
rbogdan@eti.pg.gda.pl

[1] Department of Metrology and Optoelectronics, Faculty of Electronics, Telecommunications and Informatics, Gdańsk University of Technology, 11/12 G. Narutowicza St., 80-233 Gdańsk, Poland

[2] Faculty of Microsystem Electronics and Photonics, Wrocław University of Technology, 11/17 Janiszewskiego St., 50-372 Wrocław, Poland

[3] Polish Academy of Sciences, The Szewalski Institute of Fluid-Flow Machinery, 14 Fiszera St., 80-231 Gdańsk, Poland

1 Introduction

Micro-electromechanical systems (MEMS) and nano-electromechanical systems (NEMS) provide ample sensing opportunities [1]. Due to the small dimension, low stiffness and high operating frequencies, excellent attributes and resolutions of mass change and force investigations can be achieved. For characterization of surface properties at the nanoscale, atomic force microscope (AFM) has been widely used [2–5]. Since the AFM and its applications are based on the interaction between an extremely sharp probe and the sample, the probe surface is one of the crucial concerns. Moreover, characterization at the nanoscale based on the electrical conductivity and the absence of an electronic surface barrier is beneficial. Scanning tunnelling microscopy (STM) and conductive atomic force microscopy (C-AFM) with locally performed C-AFM current–voltage measurements and Kelvin probe force microscopy (KPFM) are the most effective surface analysis methods [6–8] with atomic- or nanometre-scale spatial resolution requiring high conductivity probes.

Apart from those techniques, scanning electrochemical microscopy (SECM) provides localized information on interfacial and biological processes on challenging subjects such as cellular signalling at molecular level [9].

Several over-coated nanodevices have been proposed to mitigate conductive tip coating, including platinum silicide tips [10], silicon dioxide tip encapsulation [11], silicon carbide tips [12] and diamond or diamond-like carbon tips [13, 14]. However, noble metal-coated conductive tips exhibit disadvantages, narrow potential window or electrode fouling when applied in electrochemical nanodevices [15]. Moreover, hardness, high Young's modulus, electrical conductivity through doping, chemical inertness and high thermal conductivity of the material are crucial.

Diamond-based nanomaterials meet most of the above requirements. Moreover, diamond-coated tips are attractive for nanosensing application because they have remarkable electrochemical features which consist of chemical stability [16], a wide electrochemical window [17] and high anodic stability [18]. B-NCD achieves semi-metallic conductivity using in situ boron doping in chemical vapour deposition (CVD) process [19, 20]. Boron-doped diamond films are commonly used as an electrode material for utilization with hazardous organic compounds or sensing applications [18, 19, 21]. Moreover, due to its biocompatibility, it is a great material for sensing various kinds of proteins or DNA [22, 23].

These properties make diamond particularly attractive, also for optoelectronic devices at micro- and nanoscales that are suited for critical applications in extreme conditions [9]. Rapid technical advances now allow resolutions of 0.02 nm in depth, 50 nN in load and 50 nm in spherical diamond tip radius [24]. Niedermann et al. [25] developed chemical vapour-deposited (CVD) diamond STM and AFM probes demonstrating outstanding robustness and longevity. An emerging field is CVD diamond microelectromechanical systems (MEMS) that outperform silicon, the current material of choice in a number of critical aspects. Recently, Drew et al. [26] fabricated non-conductive hydrogen-terminated NCD-coated silicon AFM tips for photochemical force spectroscopy showing enhanced fluorescence when subjected to carboxylic acid-selective labelling conditions.

Smirnov et al. [9] developed a focused ion beam (FIB)-fabricated CVD diamond nanoprobes with a resonance frequency of 15 kHz and a nominal force constant of 0.5 N m^{-1}. The dimensions of the coated cantilever were 450, 50 and 2 μm in length, width and height, respectively. The inductively coupled plasma reactive ion etching (ICP-RIE) diamond probes were reported by Uetsuka et al. [27]. The height of their tips was in the range of 10 μm and the apex diameter as small as 50 nm, which is required for microscopic applications. Proposed fabrication processes are non-scalable and show low repeatability of fabricated structures [28]. Moreover, techniques like FIB or RIE defect diamond surface and provide co-doping by other species like gallium or fluorine influencing electrical and electrochemical properties [29].

Therefore, the authors propose here a one-step fabrication process of boron-doped nanocrystalline diamond-coated probes based on a growth of diamond on a truncated cone-shaped molybdenum stage. Such an approach changes the microwave plasma energy distribution influencing the diamond surface properties and its molecular structure [30]. To the author's best knowledge, the growth of such B:NCD films on an AFM cantilever and its effect on the change in mechanical, electrical and physical properties of these micro- and nanodevices has not been reported yet.

The B-NCD thin films have been subject to a great deal of attention due to their outstanding properties, remarkable hardness, optical transparency in a broad wavelength [31, 32], high thermal conductivity [33] as well as biocompatibility [34, 35]. Unlike the rough polycrystalline films with grain sizes above 500 nm, NCD films with typical grain sizes and surface roughness of less than 100 nm are relatively smooth showing properties close to single crystal diamond [36].

Boron-doped nanocrystalline diamond films were deposited onto silicon micro-devices using microwave plasma assisted chemical vapour deposition (MW PA CVD) method. The variation in B-NCD morphology, structure and optical parameters was particularly investigated. The evolution of the morphology was studied using a scanning electron microscope (SEM). The chemical composition of NCD film has been examined with micro-Raman spectroscopy [37]. Furthermore, the electrical parameters of boron-doped diamond films were investigated by electrical mode of AFM–Kelvin probe force microscopy (KPFM) [38].

2 Experimental details

2.1 Dip-coating nanodiamond seeding

The B-NCD films were deposited onto cantilever made of p-type (100) monocrystalline silicon. Prior to the deposition process, cantilevers were pre-treated by dip-coating in a nanodiamond slurry to initiate the seeding of diamond on a silicon surface. The seeding process consisted of immersion by an automatic mechanism for dip coating (see Fig. 1).

The silicon cantilever pre-treatment by dip-coating in dispersion consisting detonation nanodiamond (DND) in dimethyl sulphoxide (DMSO) with 0.5 % polyvinyl alcohol (PVA) was applied. The cantilever was immersed twice

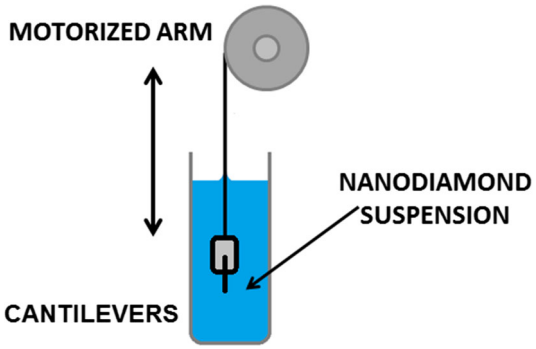

Fig. 1 Scheme of the automatic mechanism for nanodiamond seeding by dip-coating method

for 1 min in the nanodiamond suspension. The suspension was prepared in two steps. First, 1 g of solid PVA (average molar mass—18,000 g mol^{-1}) was suspended in 99 g of DMSO at temperature of 80 °C, forming 1 % w/w solution. Then, after cooling to room temperature, the 100 ml of detonation nanodiamond suspension (DMSO—0.5 % w/w) was added dropwise. Thus, the DMSO–PVA and DMSO–DND were diluted 1:1 w/w resulting in final nanodiamond concentration of 0.25 % w/w in DMSO/PVA.

2.2 Nanocrystalline diamond growth

The B-NCD films were synthesized using MW PE CVD system (SEKI Technotron AX5400S, Japan). The seeded cantilevers were placed in CVD chamber on a truncated cone-shaped molybdenum stage. The improvement of the diamond films by cone-shaped holder has been already reported by our team [30] and by other teams using other shaped holders [39, 40]. This technique enabled to grow the thin diamond films in range of 100 nm in thickness, which were fully encapsulating the substrate and exhibited high sp^3 content. To achieve high-quality, high sp^3 content films, the high microwave power densities are necessary, while the use of truncated cone-shaped substrate holder focuses strongly microwave plasma energy (see Fig. 2).

The boron level expressed as the $[B]/[C]$ ratio in the gas phase was 0 and 5000 ppm for undoped and in situ boron-doped diamond films, respectively. Diborane (B_2H_6) diluted in H_2 was used as a dopant precursor and admixture to H_2/CH_4 gas phase.

The base pressure in the chamber was 10^{-5} Torr. Then, the chamber was filled with a mixture of hydrogen, methane and additionally diborane for boron-doped film. Pressure in the chamber was kept at 50 Torr during the process with the total flow rate of gases reaching 156 sccm at methane molar ratio of 4 %.

The highly excited plasma was generated with microwave radiation (2.45 GHz) and optimized for diamond

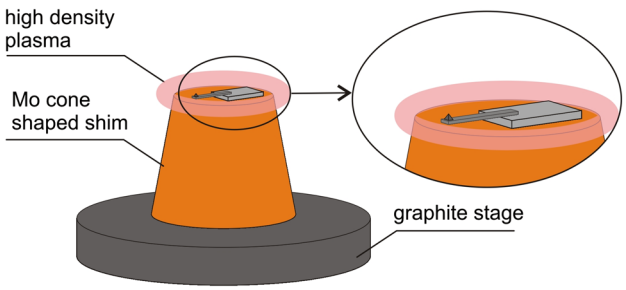

Fig. 2 Scheme of the cantilever samples positioning at the truncated cone-shaped substrate holder in microwave plasma

synthesis at power of 1000 W [41–43]. The deposition time was kept at 60 min. During the process, the molybdenum stage was heated up to 500 °C by induction heater and controlled by thermocouple.

After the growth process, the substrate temperature was slowly reduced (2 °C min^{-1}) down to room temperature. The temperature was adjusted by simultaneous lowering of the microwave power and current of induction heater. The growth time was kept at 60 min for both samples, producing nanocrystalline films of a thickness below 100 nm as reported elsewhere [30]. The deposition parameters for each sample are listed in Table 1.

The resistivity of samples was measured by a four-point probe system. The source meter (Keithley 2400, UK) was used as a current source applied to the external probes. Voltage on the internal probes was measured by VA multimeter (Appa 207, Taiwan). Each sample was measured at four surface points. The surface resistivity of 30 m Ω cm was achieved for the boron-doped diamond sample, while $\sim 10^8$ m Ω cm (value over the range of measurement system) was recorded for undoped one.

2.3 Analytical methods

2.3.1 SEM

The morphology studies were performed with a field emission gun scanning electron microscope (SEM, Helios NanoLab^{TM} 600i, FEI Co., USA). Variable pressure SEM mode (VP-SEM) was used, which allows for measuring the sample morphology regardless on its electrical conductivity. Secondary electron mode was applied with 20 kV accelerating voltage. Additionally, the SEM-based grain size at diamond surface was analysed via graphical profiling tool of the computer software for data visualization and analysis (Gwyddion, 2.40, Czech Republic) [44].

2.3.2 Raman spectroscopy

The Raman spectra were recorded at room temperature using a micro-Raman system (InVia, Renishaw, UK) and a

Table 1 The set of the fibre samples together with applied deposition parameters

Sample	H_2 (sccm)	CH_4 (sccm)	B_2H_6 (sccm)	[*B*]/[*C*] (ppm)	T_c (°C)	Time (min)
Cantilever1—undoped diamond	150	6	0	0	500	60
Cantilever2—boron-doped diamond	135	6	15	5000	500	60

514 nm argon ion laser as the excitation. Spectra were recorded in the range of 120–3300 cm^{-1} with an integration time of 5 s (10 averages) in combination with a 50× objective magnification (NA = 0.5) and 50 μm confocal aperture. The relative sp^3/sp^2 comparison of intensity of a band assigned to diamond (approx. 1332 cm^{-1}) and a wide "G" band assigned to distorted sp^2 phase (between 1520 and 1600 cm^{-1}) has been discussed.

2.3.3 AFM, KPFM

In our experiments, a commercial atomic force microscopes—Veeco Mulimode and Veeco Nanoman systems with a NanoScope 5 controller—were used. Tapping mode AFM measurements were performed using MPP-11100 probes from Bruker (force constant 40 N m^{-1}, resonant frequency 300 kHz). During KPFM measurements, PPP-EFM probes from nanosensors were applied (PtIr coating, force constant 2.8 N m^{-1}, resonant frequency 75 kHz). KPFM images were measured using two pass procedures, where the first pass determines the topography with tapping mode AFM and the second pass is performed with the probe lifted a set distance from the sample surface. During the second trace, the cantilever was not driven mechanically; instead, AC voltage of amplitude 1 V at resonance frequency was applied to the probe, and lift height was set to 25 nm. The diamond layers work function was determined taking into account the known value of the PtIr work function (5.3 ± 0.1 eV), previously calibrated on the HOPG surface and the measured contact potential difference (CPD) value.

2.3.4 Laser vibrometer

The mechanical parameters of coated cantilevers as a resonance frequency and spring constant were obtained by comprehensive system for calibration and investigation of cantilever device based on laser vibrometer (SP-S 120, SIOS GmbH, Germany). It enables measurements in the frequency range from 0 to 2.5 MHz. To determine cantilevers' effective spring constant, the system analyses an optically measured thermo-mechanical noise.

3 Results and discussion

3.1 Evolution of surface morphology and molecular structure of diamond-coated nanodevices

Figure 3 shows SEM micrographs of diamond morphology at different magnification. The diamond coating at both cantilevers was continuous and fully encapsulated the substrate. At the centre of cantilevers (Fig. 3c, d), the homogeneous film for both samples was achieved.

The images were qualitatively analysed by using a statistical procedure in Gwyddion software, which produces the crystallite size and root mean square roughness R_{RMS}. The image of undoped film at cantilever1, shown in Fig. 3c, exhibited a typical polycrystalline structure with the uniformly distributed sharp-edged crystallites [45]. As revealed by SEM imaging, the difference in width (edge-to-edge) of these crystallites reached up to ca. 250 nanometres, while the R_{RMS} value for the entire image area was approx. 170 nm.

In contrary, the boron-doped diamond at cantilever2 (see Fig. 3d) was considerably smoother and characterized by ovoid shape than the one coated by undoped NCD. The cantilever2 resulted in smaller crystallite size of ca. 150 nm and R_{RMS} value of 60 nm, but the crystallite shape is still evident.

For a conclusive interpretation of nanoindentation results, the shape of the tip has to be known precisely. Thus, further AFM studies have been performed and presented in the next subsection.

Raman spectra of the samples deposited undoped diamond thin film in free different region on cantilever are shown in Fig. 4. The 520 cm^{-1} comes from monocrystalline silicon substrate. Raman spectra of diamond film deposited on cantilever tip region show the strong diamond line at 1332 cm^{-1}.

Strong Raman spectra of amorphous band at 1580 cm^{-1} and weak diamond line at defected region can be observed. This fact can be caused by defects of the substrate during the substrate pre-treatment in the nanodiamond suspension.

Figure 5 shows Raman spectra of boron-doped diamond film deposited on the cantilever. Raman spectra present the

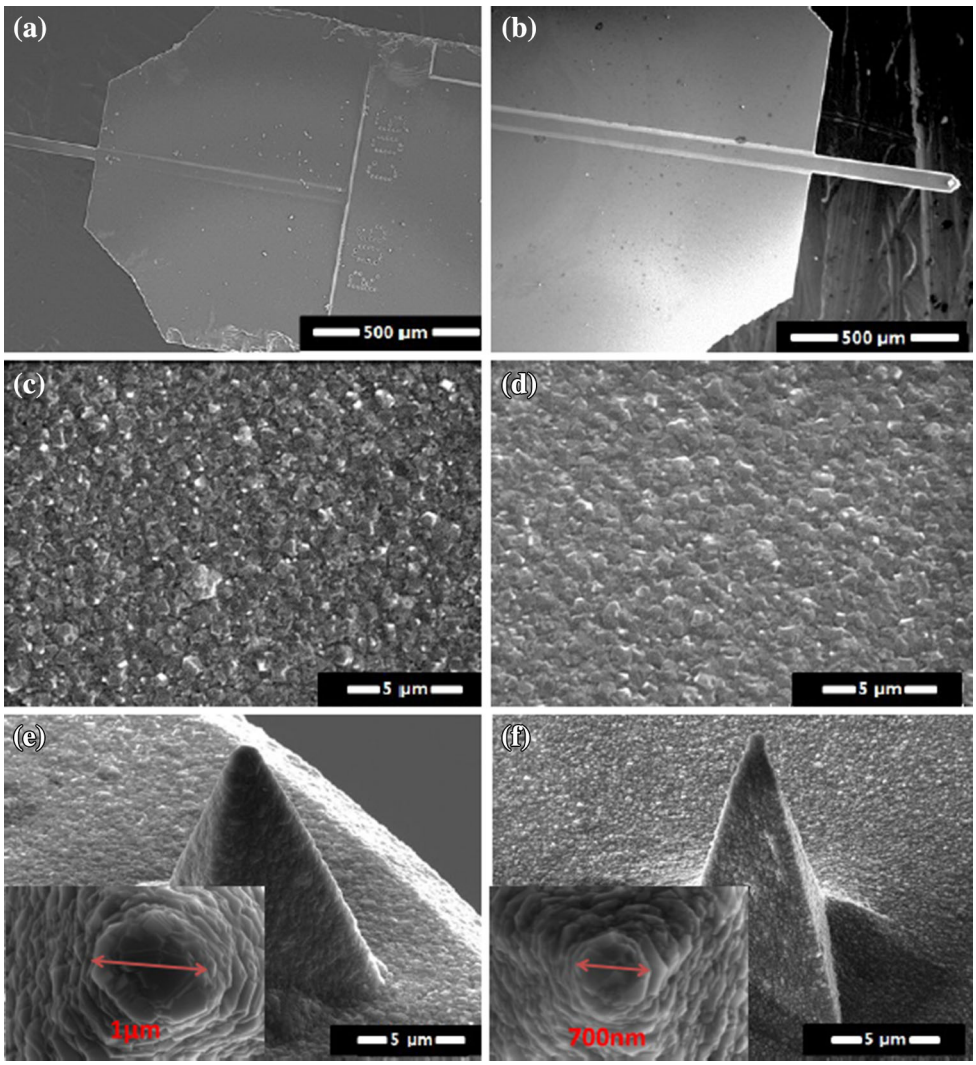

Fig. 3 SEM micrographs of Si cantilever with thin diamond films (*left* cantilever1) and boron-doped diamond films (*right* cantilever2) in different magnification: **a**, **b** 50×; **c**, **d** 10,000×; **e**, **f** 10,000×

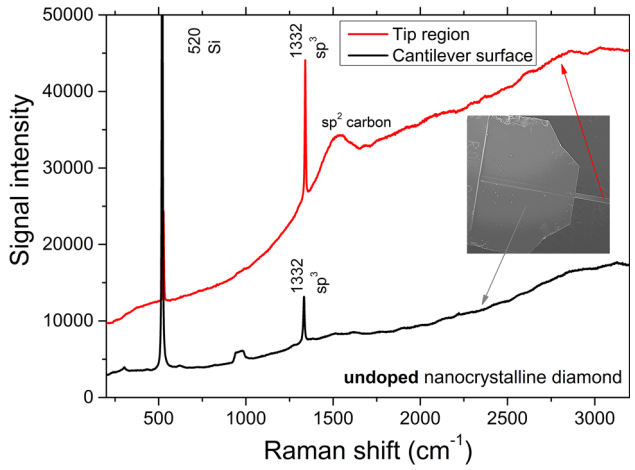

Fig. 4 Raman spectra of the silicon cantilevers coated with undoped diamond films—cantilever1

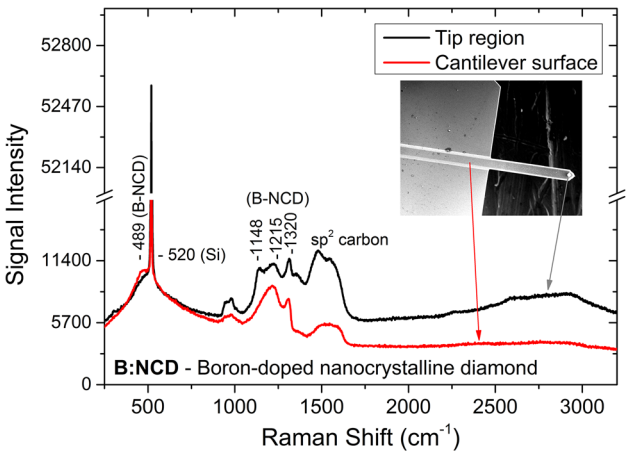

Fig. 5 Raman spectra of the silicon cantilevers coated with boron-doped diamond films—cantilever2

typical boron-doped nanocrystalline diamond lines (e.g. 1148 cm^{-1}) [30]. Ratio of diamond line and amorphous carbon lines suggest the boron-doped thin film has more defects than undoped diamond film.

Figures 6 and 7 show AFM images of boron-doped diamond and undoped films, respectively. Morphology, including rounded crystallites with different sizes and nucleation shapes, was present. The crystallite–grain size was recorded at 153 and 238 nm for boron-doped film and undoped, respectively. For an undoped film, the surface is regularly covered with crystallites which additionally enhances the surface. Moreover, the calculated values of RMS roughness of topography obtained from AFM investigations were 17 and 63 nm for boron-doped and undoped films, respectively. Thus, we could consider both fabricated samples as the typical nanocrystalline diamond (NCD) as defined by previous authors [20, 46, 47].

In summary, the AFM-estimated crystallite sizes were in agreement with SEM image analysis observations for both samples. Nevertheless, the RMS roughness values obtained by AFM and SEM showed the same trends but AFM resulted in reasonable smaller comparing to that derived by SEM profiling. This fact could be explained by low lateral resolution of SEM imaging and hence high error of such an estimation.

It could be concluded that the boron doping resulted in morphology changes (e.g. crystallite size and roughness decrease) and modified the molecular structure of diamond films (sp^2 rich area at the inter-grains regions [7]). Moreover, as suggested in literature, the boron doping can suppress the formation of microcrystalline on the surface [48].

Molecular structure modifications were registered by Raman spectra showing an increase of sp^2 bands (e.g. 1580 cm^{-1}) and peak appearance (1148 cm^{-1} NCD). Thus, the obtained morphologic (AFM and SEM) and molecular results (Raman) are consistent with each other.

Figure 8 shows a CPD histogram of the results of KPFM measurements in air condition of undoped and boron-doped diamond films on silicon substrate, while the sample was grounded. For the undoped diamond films, average CPD was 650 mV, and for boron-doped layer, it was 155 mV. Based on CPD values and known tip work function (5.3 eV for PtIr cantilever), values of work functions were calculated as 4.65 and 5.15 eV for doped and undoped diamond film, respectively. Boron doping increases the carrier density and the conductivity of the material and, consequently, the Fermi level.

Figure 9 presents the resonance frequency spectra of the cantilever before and after deposited process of boron-doped diamond film. In the presented experiment, we use standard silicon cantilever MPP-31100-10 (from Bruker) with previously measured resonant frequency and spring constant of 1.1 N m^{-1} and 21.57 kHz, respectively. After the deposition process, we note a change in both resonance frequency and spring constant of the cantilever and it was measured as 3.2 N m^{-1} and 35.87 kHz for spring constant and resonant frequency, respectively.

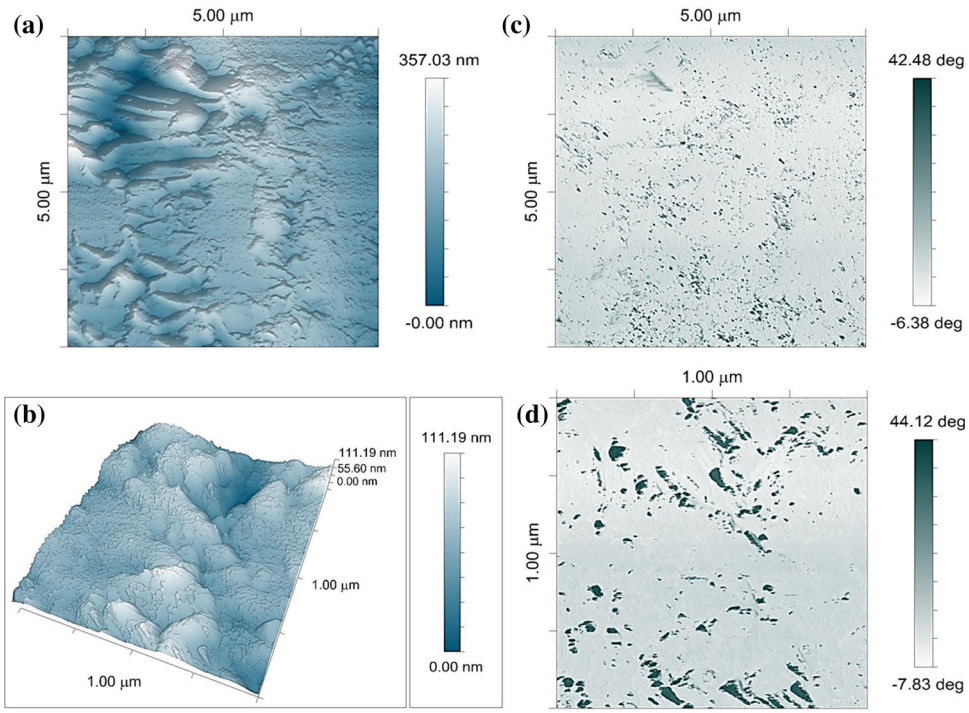

Fig. 6 Topography (**a**), 3D topography (**b**) and corresponding phase shift (**c**, **d**) images of boron-doped diamond films (cantilever2) measured in tapping mode of atomic force microscopy (TM-AFM)

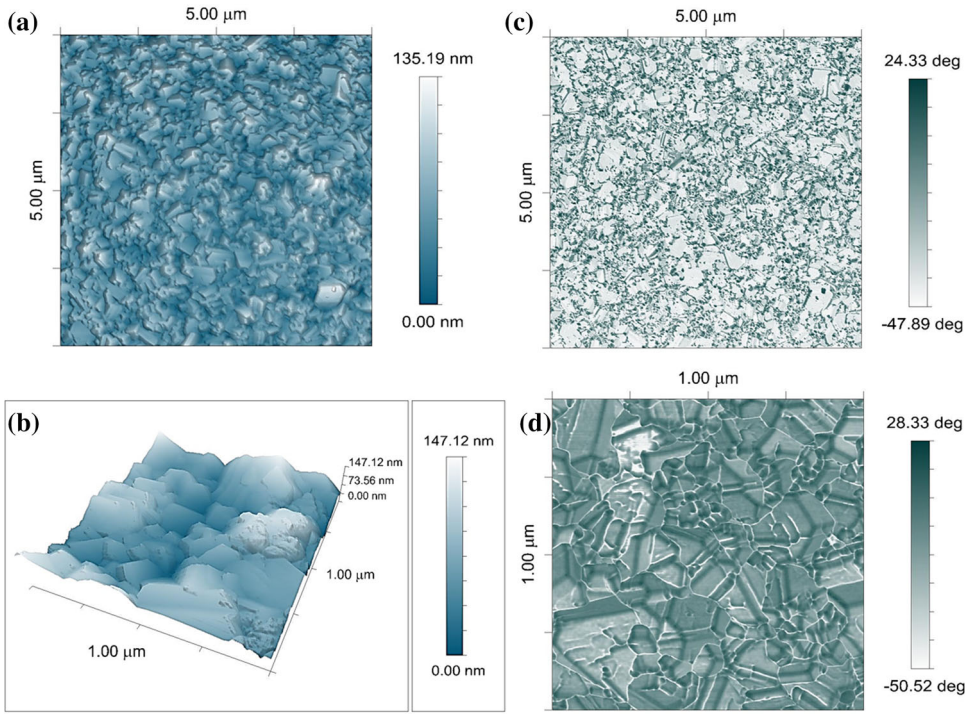

Fig. 7 Topography (**a**), 3D topography (**b**) and corresponding phase shift (**c**, **d**) images of undoped diamond films (cantilever1) measured in tapping mode of atomic force microscopy (TM-AFM)

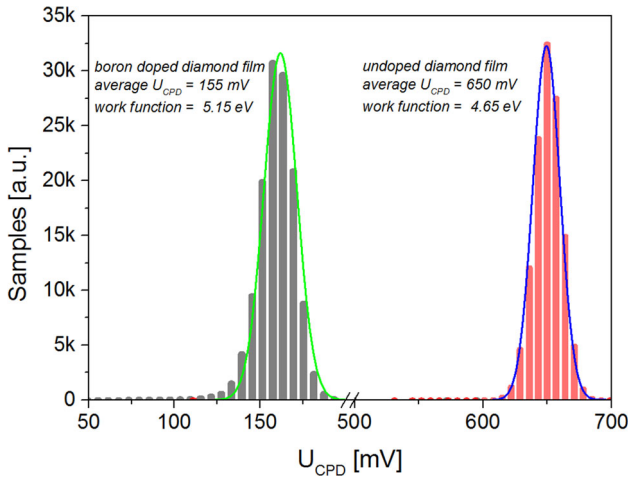

Fig. 8 CPD data histogram for both diamond films. During the measurements, the sample was grounded, and AC amplitude of electrostatic signal was set to 1 V at resonance frequency

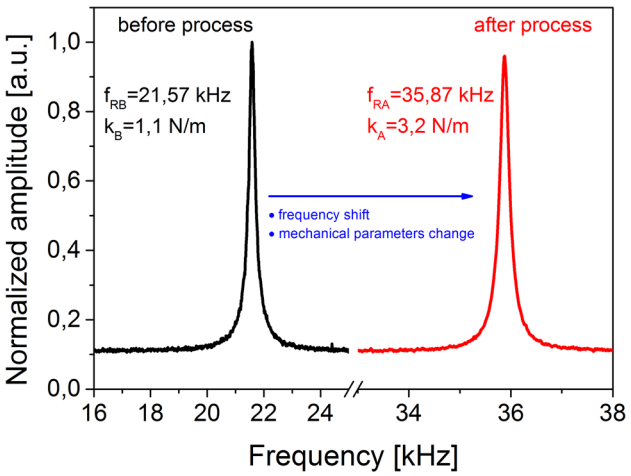

Fig. 9 The cantilever resonance frequency shift under deposited boron-doped diamond thin film on the cantilever surface

The resonance frequency increases considerably due to the change in spring constant of cantilever caused by B-NCD coating. Moreover, the spring constant increases significantly; thus, the cantilever is much stiffer due to the change in Young's modulus of structure.

The diamond films appear to be useful for covered micro- and nanomechanical devices, which can modify the mechanical and electrical properties of surface. In the case of AFM cantilever, the diamond film increases the mechanical strength of the tip and additionally the boron doping enables to conduct electrical measurements of the surface.

4 Conclusions

In this work, experimental investigation of the undoped and boron-doped diamond thin films on cantilevers is presented. Diamond-coated cantilevers are attractive tools for

micro- and nanoscale measurements and instrumentation where biological and chemical inertness are required.

The use of truncated cone-shaped substrate holder enabled to grow thin fully encapsulated B-NCD with a thickness of approx. 60 nm and RMS roughness of 17 nm. The surface morphology (crystallite size and roughness decrease) and the molecular structure of diamond films (sp^2 rich area at the inter-grains regions) were modified by boron doping.

The B-NCD results in high conductivity coverage of cantilever with surface resistivity of 30 m Ω cm and typical boron-doped nanocrystalline diamond line at 1148 cm^{-1} recorded by Raman spectroscopy.

The AFM topography showed that crystallite–grain size was 153 nm and 238 nm for boron-doped film and undoped, respectively. The KPFM studies revealed the reasonable decrease in CPD for boron-doped films comparing to an undoped one. Based on CPD values, the values of work functions were calculated as 4.65 eV and 5.15 eV for doped and undoped diamond film, respectively. This fact proves that boron doping increased the carrier density, the conductivity and consequently the Fermi level. Moreover, we have noted that the B-NCD coating changed both resonance frequency and spring constant of cantilever.

Surface modification of the micro- and nanocantilevers is a very interesting opportunity to change mechanical, electrical and physical properties of these micro- and nanodevices. Modified cantilevers can be attractive tools in atomic force microscopes (AFM) as scanning probes in biosensor applications.

Acknowledgments This work was supported by the Polish National Science Center (NCN) under the Grant Nos. 2011/03/D/ST7/03541 and 2014/14/M/ST5/00715. The DS funds of Faculty of Electronics, Telecommunications and Informatics of the Gdansk University of Technology are also acknowledged. The work was partially supported by the Foundation for Polish Science within the TEAM Programme FoMaMet (Grant No. TEAM/2012-9/3), co-financed by the European Regional Development Fund.

References

1. S.E. Lyshevski, *MEMS and NEMS: Systems, Devices, and Structures*, 1st edn. (CRC Press, Boca Raton, 2002)
2. G. Haugstad, *Atomic Force Microscopy: Understanding Basic Modes and Advanced Applications*, 1st edn. (Wiley, Hoboken, 2012)
3. K. Waszczuk, G. Gula, M. Swiatkowski, J. Olszewski, W. Herwich, Z. Drulis-Kawa, J. Gutowicz, T. Gotszalk, Sens. Actuators B Chem. **170**, 7 (2012)
4. G. Jóźwiak, D. Kopiec, P. Zawierucha, T. Gotszalk, P. Janus, P. Grabiec, I.W. Rangelow, Sens. Actuators B Chem. **170**, 201 (2012)
5. K. Waszczuk, T. Piasecki, K. Nitsch, T. Gotszalk, Sens. Actuators B Chem. **160**, 517 (2011)
6. M. Moczała, D. Kopiec, A. Sierakowski, R. Dobrowolski, P. Grabiec, T. Gotszalk, Microelectron. Eng. **119**, 164 (2014)
7. A. Zieliński, R. Bogdanowicz, J. Ryl, L. Burczyk, K. Darowicki, Appl. Phys. Lett. **105**, 131908 (2014)
8. K. Gajewski, D. Kopiec, M. Moczała, A. Piotrowicz, M. Zielony, G. Wielgoszewski, T. Gotszalk, W. Strupiński, Micron **68**, 17 (2015)
9. W. Smirnov, A. Kriele, R. Hoffmann, E. Sillero, J. Hees, O.A. Williams, N. Yang, C. Kranz, C.E. Nebel, Anal. Chem. **83**, 4936 (2011)
10. H. Bhaskaran, A. Sebastian, M. Despont, I.E.E.E. Trans, Nanotechnol. **8**, 128 (2009)
11. H. Bhaskaran, A. Sebastian, U. Drechsler, M. Despont, Nanotechnology **20**, 105701 (2009)
12. M.A. Lantz, B. Gotsmann, P. Jaroenapibal, T.D.B. Jacobs, S.D. O'Connor, K. Sridharan, R.W. Carpick, Adv. Funct. Mater. **22**, 1639 (2012)
13. H.J. Kim, N. Moldovan, J.R. Felts, S. Somnath, Z. Dai, T.D.B. Jacobs, R.W. Carpick, J.A. Carlisle, W.P. King, Nanotechnology **23**, 495302 (2012)
14. J. Liu, D.S. Grierson, N. Moldovan, J. Notbohm, S. Li, P. Jaroenapibal, S.D. O'Connor, A.V. Sumant, N. Neelakantan, J.A. Carlisle, K.T. Turner, R.W. Carpick, Small **6**, 1140 (2010)
15. D.P. Manica, Y. Mitsumori, A.G. Ewing, Anal. Chem. **75**, 4572 (2003)
16. G.M. Swain, A.B. Anderson, J.C. Angus, MRS Bull. **23**, 56 (1998)
17. J. Iniesta, P.A. Michaud, M. Panizza, G. Cerisola, A. Aldaz, C. Comninellis, Electrochim. Acta **46**, 3573 (2001)
18. D. Gandini, E. Mahé, P.A. Michaud, W. Haenni, A. Perret, C. Comninellis, J. Appl. Electrochem. **30**, 1345 (2000)
19. R. Bogdanowicz, J. Czupryniak, M. Gnyba, J. Ryl, T. Ossowski, M. Sobaszek, E.M. Siedlecka, K. Darowicki, Sens. Actuators B Chem. **189**, 30 (2013)
20. W. Gajewski, P. Achatz, O.A. Williams, K. Haenen, E. Bustarret, M. Stutzmann, J.A. Garrido, Phys. Rev. B **79**, 045206 (2009)
21. J. Xu, G.M. Swain, Anal. Chem. **70**, 1502 (1998)
22. K. Pecková, J. Musilová, J. Barek, Crit. Rev. Anal. Chem. **39**, 148 (2009)
23. C. Prado, G.-U. Flechsig, P. Gründler, J.S. Foord, F. Marken, R.G. Compton, Analyst **127**, 329 (2002)
24. N. Yu, A.A. Polycarpou, J. Vac. Sci. Technol. B **22**, 668 (2004)
25. P. Niedermann, W. Hänni, D. Morel, A. Perret, N. Skinner, P.-F. Indermühle, N.-F. de Rooij, P.-A. Buffat, Appl. Phys. A **66**, S31 (1998)
26. M.E. Drew, A.R. Konicek, P. Jaroenapibal, R.W. Carpick, Y. Yamakoshi, J. Mater. Chem. **22**, 12682 (2012)
27. H. Uetsuka, T. Yamada, S. Shikata, Diam. Relat. Mater. **17**, 728 (2008)
28. M. Moriarty, J. Blackwood, J. Arjavac, Microsc. Microanal. **16**, 204 (2010)
29. A. Eifert, P. Langenwalter, J. Higl, M. Lindén, C.E. Nebel, B. Mizaikoff, C. Kranz, Electrochim. Acta **130**, 418 (2014)
30. M. Sobaszek, Ł. Skowroński, R. Bogdanowicz, K. Siuzdak, A. Cirocka, P. Zięba, M. Gnyba, M. Naparty, Ł. Gołuński, P. Płotka, Opt. Mater. **42**, 24 (2015)
31. X. Checoury, D. Néel, P. Boucaud, C. Gesset, H. Girard, S. Saada, P. Bergonzo, Appl. Phys. Lett. **101**, 171115 (2012)

32. J. Stotter, S. Haymond, J.K. Zak, Y. Show, Z. Cvackova, G.M. Swain, Interface **12**, 33 (2003)
33. A.V. Sukhadolau, E.V. Ivakin, V.G. Ralchenko, A.V. Khomich, A.V. Vlasov, A.F. Popovich, Diam. Relat. Mater. **14**, 589 (2005)
34. P. Bajaj, D. Akin, A. Gupta, D. Sherman, B. Shi, O. Auciello, R. Bashir, Biomed. Microdevices **9**, 787 (2007)
35. M. Amaral, A.G. Dias, P.S. Gomes, M.A. Lopes, R.F. Silva, J.D. Santos, M.H. Fernandes, J. Biomed. Mater. Res. A **87A**, 91 (2008)
36. O.A. Williams, A. Kriele, J. Hees, M. Wolfer, W. Müller-Sebert, C.E. Nebel, Chem. Phys. Lett. **495**, 84 (2010)
37. R. Bogdanowicz, A. Fabianska, L. Golunski, M. Sobaszek, M. Gnyba, J. Ryl, K. Darowicki, T. Ossowski, S.D. Janssens, K. Haenen, E.M. Siedlecka, Diam. Relat. Mater. **39**, 82 (2013)
38. W. Melitz, J. Shen, A.C. Kummel, S. Lee, Surf. Sci. Rep. **66**, 1 (2011)
39. A.B. Muchnikov, A.L. Vikharev, A.M. Gorbachev, D.B. Radishev, Diam. Relat. Mater. **20**, 1225 (2011)
40. A.B. Muchnikov, A.L. Vikharev, A.M. Gorbachev, D.B. Radishev, V.D. Blank, S.A. Terentiev, Diam. Relat. Mater. **19**, 432 (2010)
41. R. Bogdanowicz, M. Gnyba, P. Wroczyński, J. Phys. IV Proc. **137**, 57 (2006)
42. R. Bogdanowicz, M. Gnyba, P. Wroczyński, B.B. Kosmowski, J. Optoelectron. Adv. Mater. **12**, 1660 (2010)
43. R. Bogdanowicz, Acta Phys. Pol. A **114**, A33 (2008)
44. D. Nečas, P. Klapetek, Open Phys. **10**, 181 (2012)
45. R. Bogdanowicz, M. Sawczak, P. Niedzialkowski, P. Zieba, B. Finke, J. Ryl, J. Karczewski, T. Ossowski, J. Phys. Chem. C **118**, 8014 (2014)
46. Y. Show, M.A. Witek, P. Sonthalia, G.M. Swain, Chem. Mater. **15**, 879 (2003)
47. P.W. May, W.J. Ludlow, M. Hannaway, P.J. Heard, J.A. Smith, K.N. Rosser, Diam. Relat. Mater. **17**, 105 (2008)
48. S. Mingji, W. Zhanguo, L. Shiyong, P. Wenbo, X. Haibo, Z. Changsha, Z. Xiangbo, J. Semicond. **30**, 063001 (2009)